2015년 2월

석사학위 논문

Synthesis of Silver Hollow Structure from Silver Oxide Template, and Predicting the Radius of Assembled Structure: Experimental and Theoretical New Approach

조 선 대 학 교 대 학 원

화 학 과

조 지 희

산화은 템플레이트를 이용한 속이 빈 은 구조체의 합성과 자기조립된 구조체의 반경 예측을 위한 실험적, 이론적인 새로운 접근법

Synthesis of Silver Hollow Structure from Silver Oxide Template, and Predicting the Radius of Assembled Structure: Experimental and Theoretical New Approach

2015년 2월 25일

조 선 대 학 교 대 학 원

화 학 과

조 지 희

산화은 템플레이트를 이용한 속이 빈 은 구조체의 합성과 자기조립된 구조체의 반경 예측을 위한 실험적, 이론적인 새로운 접근법

지도교수 임 종 국

이 논문을 이학석사학위신청 논문으로 제출함.

2014년 10월

조 선 대 학 교 대 학 원

화 학 과

조 지 희

조지희의 석사학위논문을 인준함

위원장 조선대학교 교수 손 홍 래 (인)

위 원 조선대학교 교수 김 호 중 (인)

위 원 조선대학교 교수 임 종 국 (인)

2014년 11월

조 선 대 학 교 대 학 원

TABLE OF CONTENTS

Chapter Two. A New Approach to Obtain Correct and Simplified Equation Applied to inner Space Assessment for Capsule-like Superstructures

Abstract

Synthesis of Silver Hollow Structure from Silver Oxide Template, and Predicting the Radius of Assembled Structure: Experimental and Theoretical New Approach

Jo, Jihee
Advisor : Prof. Lim, Jong Kuk, Ph.D,
Department of Chemistry,
Graduate School of Chosun University

제 1장.

현재까지 다양한 나노입자를 합성하기 위한 여러 가지 방법들이 개발되어 왔는데, 그 중 효과적인 방법 중 하나는 “템플레이트 기반 접근법”이다. 이 방법에서는 나노입자의 크기나 모양이 사용된 템플레이트의 크기와 모양에 의해 제한되기 때문에, 템플레이트를 사용하지 않았을 경우 보다 더 다양한 형태 다양한 크기의 나노입자를 손쉽게 만들 수 있다는 장점을 가지고 있다.

예를 들어, 은 나노입자를 템플레이트로 이용하여 속이 빈 금 나노입자를 쉽게 만들 수 있다. 은 나노입자를 금 이온이 녹아있는 용액 안에 넣었을 때, 은 나노입자는 쉽게 은 이온으로 산화되어 용해된다. 동시에 금 이온은 환원되어 은 나노입자 부근에 증착되는데, 이러한 일련의 방식을 거쳐 은의 크기와 모양을 따르는 속이 빈 금 나노입자

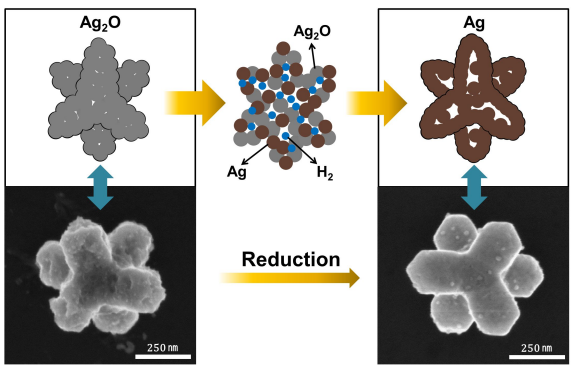

가 형성되게 된다. 이 방식은 쉽고 간단하게 속이 빈 금 나노입자를 만들 수 있다는 장점이 있지만 은 자체가 템플레이트로 이용되고 있기 때문에, 이 방법을 이용하여 속이 빈 은 나노입자를 합성하기는 어렵다는 단점을 가지고 있다.

이 논문에서, 우리는 할로우 실버 나노구조를 만들기 위해 산화은을 템플레이트로 이용하는 방법을 소개하고자 한다. 먼저 우리는 새로운 리간드를 이용하여 산화은(Ag_2O) 헥사포드(hexapod)를 합성하였고, 그것을 속이 빈 은 헥사포드를 합성하기 위한 템플레이트로써 이용하였다. 산화은 헥사포드는 소듐보로하이드라이드($NaBH_4$)를 이용하여 쉽게 은 헥사포드로 환원될 수 있는데 환원과정에서 헥사포드의 크기와 모양이 유지됨을 확인하였고, 부분적으로 속이 빈 은 헥사포드입자가 형성됨을 다양한 분석학적 기술을 동원하여 확인하였다.

제 2장.

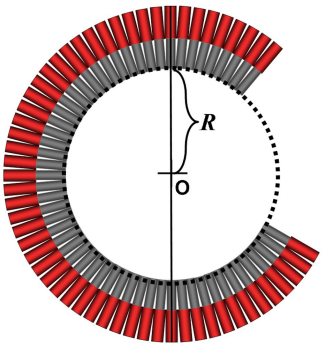

with assumption

$$R = \frac{d_{Au}}{\alpha} - l_{PPy}, \quad \alpha = 2\tan^{-1}\left(\Delta d / 2l_{PPy}\right)$$

$$R = \frac{d_{PPy} + \Delta d\cos(\alpha/2)}{\alpha} - l_{PPy}, \; \alpha = 2\tan^{-1}\left(\Delta d / 2l_{PPy}\right)$$

without assumption

$$R = \frac{d_{PPy} \cdot l_{PPy}}{\Delta d}$$

폴리피롤-골드로 구성된 세그먼트 나노와이어들은 양극산화 알루미나(AAO) 템플레이트를 이용하여 쉽게 만들어 질 수 있는데, 이러한 세그먼트 나노와이어들은 특정 조건에서 휘어진 자기조립 거대구조체를 형성하게 된다. 자기조립 거대구조체는 재료들을 담을 수 있는 내부 공간을 가진 캡슐과 같은 형태로 디자인되어질 수 있고, 또한 그들의 개폐가 외부 자극에 의해 통제되어질 수 있기 때문에, 이 구조는 개인의 아이디어에 따라 다양한 방면에 응용되어질 수 있을 것이다. 이러한 응용을 위해서 우리가 알아야 할 유용한 정보 중 하나는 캡슐의 내부 공간 부피이다. 그리고 내부 공간의 부피

는 J. K. Lim (Bull. Korean Chem. Soc. 33, 2699 (2012))에 의해 제안된 일반적인 식을 이용하여 계산되어질 수 있다. 그러나 여기서 제안된 식은 몇 가지 가정을 기반으로 유도가 된 식인데, 본 논문에서 우리는 이러한 가정 없이 캡슐의 내부 공간 부피를 계산할 수 있는 새로운 접근법을 소개하고자 한다. 여기서 새롭게 소개된 공식을 이용하여 캡슐형태의 거대구조체의 내부 공간 부피를 계산하고 이전 공식을 이용하여 얻어진 결과와 비교한다.

Chapter One.

The Synthesis of Silver Hexapods using Silver Oxide Hexapods as Templates

1. Abstract

Many different methods have been developed to synthesize a variety of nanoparticles. One powerful method to make nanoparticles is the template-based approach. Because the size or shape of nanoparticles is confined by such templates, more diverse nanoparticles can be obtained using the template-based method. For example, hollow gold (Au) nanostructures are easily fabricated using silver (Ag) nanoparticles as templates. Ag nanoparticles in a solution containing Au ions are readily oxidized to Ag ions and dissolved, while Au ions are reduced and deposited in the vicinity of the Ag nanoparticles. Because the reactivity of Au ions is lower than that of Ag ions, this exchange reaction readily occurs, resulting in hollow Au nanostructures. In this paper, we use an unprecedented approach to make hollow Ag nanostructures. We synthesize Ag_2O hexapods using a new method and use them as templates for the synthesis of hollow Ag hexapods. Interestingly, the synthesized Ag_2O hexapods are reduced by sodium borohydride and are quickly transformed into Ag hexapods, keeping their shape. We show experimental evidence for this unprecedented shape-retaining reduction of semiconductors into metals, and propose a plausible mechanism.

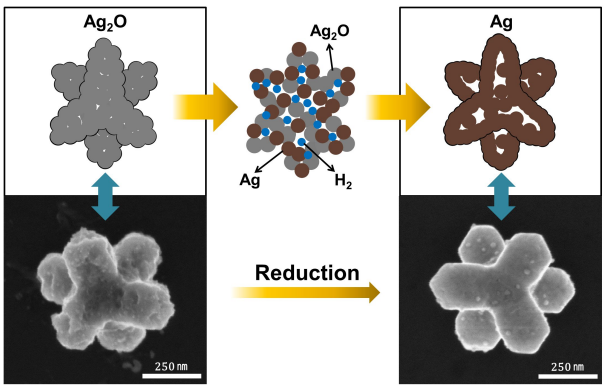

2. Introduction

Metal nanoparticles can be applied in many different areas such as biological diagnostics[1], chemical sensing[2], plasmonics[3], electronics[4], therapeutics[5,6], and catalysis[7,8]. In the past few decades, many synthetic methods have been developed to control their size, shape, and composition, and techniques now exist for preparing gold (Au) or silver (Ag) spheres[9], wires[10,11], triangular prisms[12], cubes[13], triangular bipyramids[14], tetrahedra[15], octahedra[16], decahedra[17], or disks[18,19]. One of these novel methods developed to synthesize metal nanoparticles is the template-based approach. A variety of templates including porous membranes[11], micelles[20], polystyrene mesospheres[19], block copolymers[21], or even metal nanoparticles[22] have been successfully used for this process. Since the growth of nanoparticles is confined to such templates, this template-based method allows one to better tailor the shape, size, and composition of nanoparticles[23]. For example, Xia and coworkers demonstrated that hollow Au nanostructures are easily synthesized by a "galvanic replacement reaction" where Ag nanoparticles act as templates. This method is based on the different reactivity of Au and Ag and the replacement reaction between them. When placed in a solution containing Au ions, Ag nanoparticles are easily oxidized and dissolved into the solution, while Au ions are reduced and deposited in the vicinity of the Ag nanoparticles instead of the dissolved Ag ions, because of the higher standard reduction potential of Au ions. The reduced Au nanoparticles form a shell-like structure around the Ag nanoparticles, and finally form different hollow Au nanostructures with a variety of shapes. The authors also expected that it is possible to make hollow Pt and Pd nanostructures using the same technique, because the standard reduction potentials of Pt and Pd are also higher than that of Ag. As expected, they successfully synthesized hollow Pt and Pd nanotubes. This galvanic replacement

method is appropriate for fabricating hollow Au, Pt, or Pd nanostructures, but it is difficult to use the same technique to make hollow Ag nanostructures, because Ag nanoparticles themselves are used as the template in this method, and the standard reduction potential of Ag is relatively low. Therefore, only a few papers on the synthesis of hollow Ag nanostructures have been published[24,25].

Herein, we introduce an unprecedented approach to make hollow Ag nanostructures. This method is based upon the idea that Ag_2O could be reduced to Ag. Because the reduction of Ag_2O to Ag is well known reaction[25,26], and can be accomplished by hydrogen gas, or sodium borohydride ($NaBH_4$), one may doubt if morphology-controlled Ag_2O particles may transform into Ag particles while retaining their size and shape. As an example, Yang et al. demonstrated that it is possible to fabricate size adjusted hollow Ag spheres by reducing Ag_2O spheres. The authors used silver oxide (Ag_2O) spheres as templates and reduced them using a chemical reducing agent ($NaBH_4$) to finally transform the Ag_2O spheres into hollow Ag spheres. They showed that the size of the hollow Ag spheres can be adjusted according to the initial size of the Ag_2O spheres[25].

In this article, we use morphology-controlled Ag_2O quasi-hexapods as templates instead of spheres and reduce them to Ag hexapods. To make Ag_2O hexapods, a facile and novel wet chemical method is employed, and subsequently, Ag_2O hexapods are transformed into Ag hexapods through the reduction of Ag_2O using $NaBH_4$. Interestingly, both the shape and size of the hexapods are sustained during the reduction. A plausible mechanism for this process is given with supporting evidence and discussed.

3. Experiment

3.1.Chemicals

Silver nitrate ($AgNO_3$, ≥99.0%, Aldrich), trisodium citrate dihydrate (TSC, $C_6H_5Na_3O_7{\cdot}2H_2O$, 99.0%, OCI Ltd.), bis(*p*-sulfonatophenyl) phenylphosphine dehydrate dipotassium (BSPP, 97%, Aldrich), sodium hydroxide (NaOH, 98.0%, OCI Ltd.), and sodium borohydride ($NaBH_4$, 99%, Aldrich) were used without further purification, and highly purified deionized (DI) water (18.2MΩcm), produced using QPAK1 (MILLI Pore), was used for all aqueous solutions.

3.2.Synthesis of silver (Ag) and silver oxide (Ag_2O)hexapods

The synthetic procedure and the concentration of each chemical are represented in Scheme 1. Ag_2O hexapods were firstly synthesized, and then they were transformed into Ag hexapods. In a typical experiment, the solution for the synthesis of Ag_2O hexapods was prepared by adding $AgNO_3$ (10 mM, 0.65 mL), trisodium citrate dihydrate (TSC) (100 mM, 0.32 mL), and freshly prepared bis(*p*-sulfonatophenyl) phenylphosphine dehydrate dipotassium (BSPP) (10 mM, 0.5 mL) into DI water (18.5 mL) (Stage 1 in Scheme 1). NaOH (100 mM, 1 mL) was further added into solution ② to adjust pH of the solution to 11.0 ± 0.5 using pH indicator paper (Type CF, Whatman), and the colorless solution changed to a light yellow solution (Stage 2 in Scheme 1). Solution ③ was wrapped in aluminum foil to prevent exposure to light and cured at room temperature without stirring for 1 or 2 h. For the analysis of the Ag_2O hexapods, solution ③ was centrifuged at 9600 rpm for 10 - 20 min (Centrifuge Minispin Plus; Eppendorf), and the precipitates were collected and washed with DI water several times. To transform the Ag_2O hexapods into Ag hexapods, freshly prepared $NaBH_4$ (5 mM, 2 mL) was rapidly added to solution ③ without stirring. The color of the solution changed slightly, from light yellow to yellow

(Stage 3 in Scheme 1). The final solution, ④, was placed on an experimental bench for 14 - 115 h in the dark at room temperature without stirring and then centrifuged at 9600 rpm for 10 - 20 min to collect the precipitates.

3.3. Characterization

The morphology of the Ag or Ag_2O hexapods was observed using field emission scanning electron microscopy (FE-SEM, S-4800; Hitachi), and their composition was analyzed using energy dispersive spectroscopy (EDS), equipped on the same FE-SEM instrument. For those measurements, the precipitates of Ag or Ag_2O hexapods were collected from the colloidal solution using a centrifuge (Centrifuge Minispin Plus; Eppendorf) and drop casted on pre-cleaned Si wafers. For identifying Ag and Ag_2O, X-ray diffraction (XRD) spectra were measured with X'pert PRO MPD diffractometer (PAnalytical) using Cu Kα radiation, and X-ray photoelectron spectroscopy (XPS, Axis-NOVA; Kratos Inc.) with an Al Kα source was used. The optical properties were investigated using a UV-Vis spectrophotometer (Optizen 3220UV; MECASYS) for a fixed path length (1 cm). The inner structure and selected area electron diffraction (SAED) pattern of the Ag hexapods were obtained using transmission electron microscopy (TEM, JEM-3010; JEOL) with an acceleration voltage of 300 kV on copper grids coated with carbon films.

4. Results and Discussion

The synthetic method for silver oxide (Ag_2O) particlesis well known; however, a morphology-controlled synthesis was only recently reported[27-29]. In the classical method, Ag_2O particles are easily prepared as precipitates from a solution containing both silver nitrate ($AgNO_3$) and sodium hydroxide (NaOH) (Eq.(1)).

$$2AgNO_3(aq) + 2NaOH(aq) \rightarrow Ag_2O(s)\downarrow + H_2O(l) + 2Na^+(aq) + 2NO_3^-(aq) \quad (1)$$

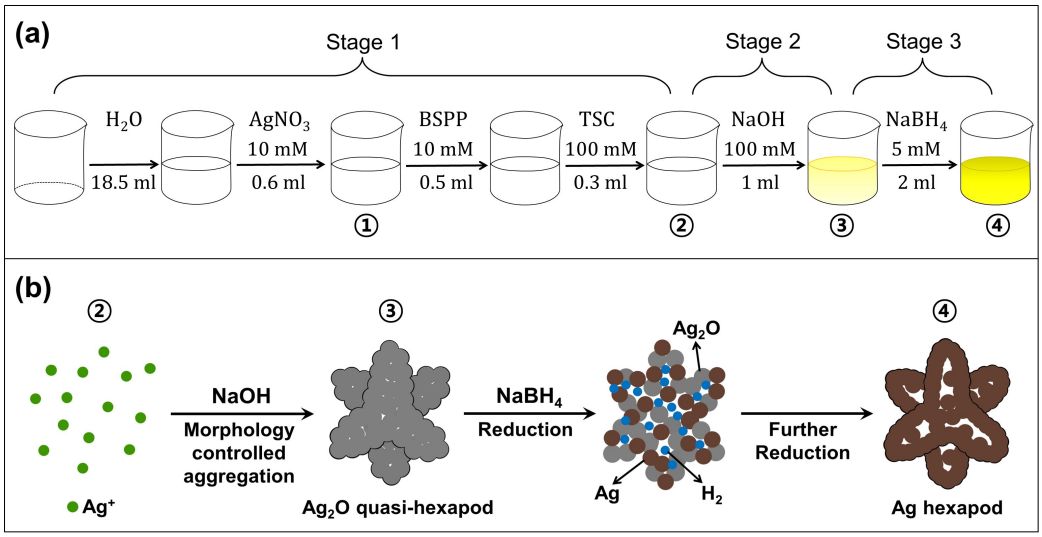

Scheme 1. The synthetic procedure and formation mechanism of Ag hexapods are illustrated in (a), and (b), respectively. The synthetic route can be broken down into three stages according to the color of the solution: (a). Solution "②" contains Ag ions and is transparent and colorless. When NaOH is added to solution "②", the color of the solution changes to light-yellow (solution "③"). In solution "③", the Ag_2O nanoparticles are produced from Ag ions, and Ag_2O quasi-hexapods are prepared by morphology-controlled aggregation of small Ag_2O nanoparticles. Finally, added $NaBH_4$ transforms the Ag_2O quasi-hexapods into Ag hexapods, and the color of the solution changes from light-yellow to yellow (solution"④").

Since this reaction rate is too fast to control the shape and size of Ag_2O particles, it is difficult to obtain Ag_2O particles with a controlled shape and size. In recent years, many different shapes of Ag_2O particles have been synthesized by decreasing there action rate. In these papers, authors used ammonia (NH_3) orpyridine (Py) as a ligand (L) to form coordinate bond with silver ions, and finally complex ions ($Ag(NH_3)_2^+$, or $Ag(Py)_2^+$) (Eq.(2)).

$$2AgNO_3(aq) + 4L(aq) \rightarrow 2Ag(L)_2^+(aq) + 2NO_3^-(aq), \text{ where L = } NH_3 \text{ or Py} \quad (2)$$

The reaction of complex ions with NaOH at a retarded rate enables the growth of morphology-controlled Ag_2O particles.

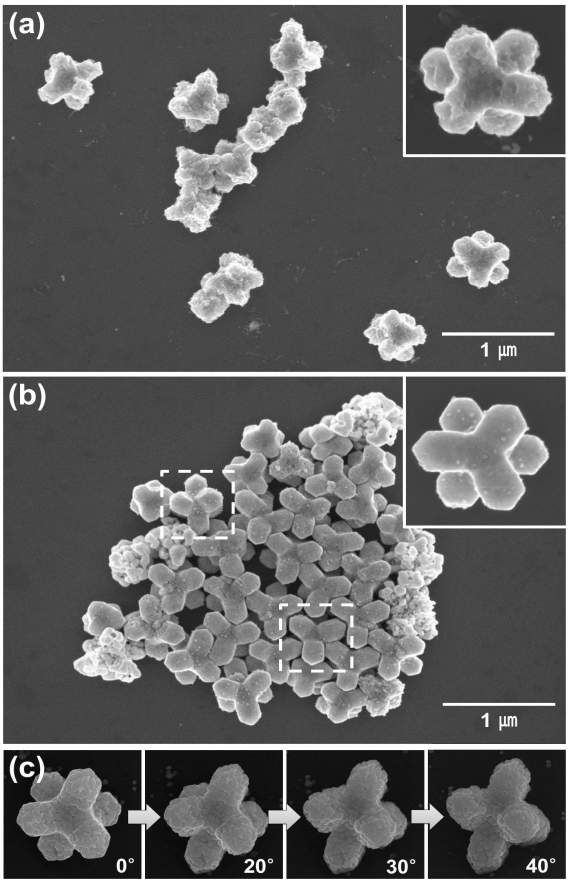

Figure 1. Scanning electron micrograph of Ag_2O quasi-hexapods (a) and Ag hexapods (b). Both insets clearly show that the surface and edge of Ag hexapods are smooth and more sharp than that of Ag_2O hexapods, which means that Ag hexapods have a more perfect crystalline phase than Ag_2O hexapods. A series of tilted images (c) reveal that the two particles highlighted in dashed squares in (b) have identical shape, and the tilt angle of ~40° indicates that the shape of the particles is a hexapod.

In our experiment, bis(*p*-sulfonatophenyl) phenylphosphine dehydrate dipotassium (BSPP) was used as a ligand instead of ammonia or pyridine, because BSPP easily forms a complex ion with silver ions, $Ag(BSPP)^+$,and ammonia and pyridine are harmful[30]. The complex ion $Ag(BSPP)^+$ gently reacts

with NaOH, and Ag_2O quasi-hexapods are finally obtained (Scheme 1b, Fig. 1a and its inset). Because the surface of the particle is very rough, and the shape of the particle is not well defined, as shown in Fig. 1a, it can be considered that the Ag_2O quasi-hexapods are formed via aggregation of small Ag_2O nanoparticles, similar to the Ag_2O quasi-spheres published in Ref. 25. This hypothesis is clearly represented in Fig. S1, which shows a partially broken Ag_2O hexapod with a big hole in the center of it. When the aqueous solution containing the as-prepared Ag_2O hexapods are dropped on to substrates and placed under vacuum to rapidly evaporate the water solvent, H_2O is rapidly evaporated from the inside of the Ag_2O hexapods, and this rapid evaporation of H_2O leads to the incomplete aggregation of the small Ag_2O nanoparticles, that are clearly seen on the surface of the Ag_2O hexapods and in the vicinity of the big hole.

Generally, Ag_2O can be transformed into Ag through chemical reduction using a reducing agent (e.g., $NaBH_4$). Since a previous report[25] showed that Ag_2O can act as a template for the synthesis of hollow Ag spheres of tunable size, one may doubt if the hexapod shape of the Ag_2O particles could be maintained during the reduction process (Scheme 1b). In this experiment, the final product (Ag hexapods reduced from Ag_2O hexapods) was obtained by adding $NaBH_4$ into solution ③, containing Ag_2O hexapods (Scheme 1b), and their morphology was investigated using FE-SEM (Fig. 1b and its inset). Interestingly, the shape of the Ag_2O hexapods was not changed but maintained during the reduction process, that is, the reduction of Ag_2O into Ag occurs with a preservation of the particle shape. As shown in Fig. 1b, the shape of the reduced Ag particles was also hexapod, identical in shape to the Ag_2O hexapod (Fig. 1a), but the surface roughness and edge angle are some what different. Compared with Ag_2O hexapods, Ag hexapods have a much clearer surface and sharper edge angle, which means that the crystallinity of the Ag hexapods is better than that

of the Ag_2O hexapods. In Fig. 1b, there are two different shaps of particles that are highlighted as dashed squares. Tilted SEM images revealed that the two different shapes of particles have identical morphology (Fig. 1c). The difference of angle between the two different images in Fig. 1c is ~40°, which reconfirms that the particle shape is hexapod. It should be noted that, in the overall reaction, the concentration of each chemical is very critical in forming Ag hexapods and for their yield. For example, if 0.4 mL BSPP solution (less than 0.5 mL) is added into solution ① in Scheme 1a, the concentration of particles in the final solution ④ is high, but the shape of the particles is non-hexapod (Fig. S2a). When the added volume of BSPP solution is increased from 0.4 to 0.5 mL, the yield of the particles decreases, but their shape is well-defined hexapods (Fig. S2b). If more than 0.5 mL BSPP solution is added, the yield is too low to collect precipitates. The pH of the solution is also an important parameter in controlling the morphology of the final product. The Ag hexapods are produced only in highly alkaline conditions (pH >11). The size of the Ag_2O hexapods varies from ~300 nm to ~1 μm, depending on the batch, because their size is very sensitive to the experimental environment. Although the Ag_2O hexapods are synthesized under the same conditions, their size could be different by a slight variation of the experimental conditions. Contrary to the Ag_2O hexapods, the size of the Ag hexapods mostly follows the size of the Ag_2O hexapods. This is a reasonable consequence from our suggested mechanism (Scheme 2). According to our suggested mechanism in Scheme 1b, Ag_2O hexapods play a role as a template for the synthesis of Ag hexapods, thus the size of the Ag hexapods should be similar to that of the Ag_2O hexapods.

Because the SEM images do not give any information on the chemical composition of the Ag_2O and Ag hexapods, it is difficult to ascertain with only

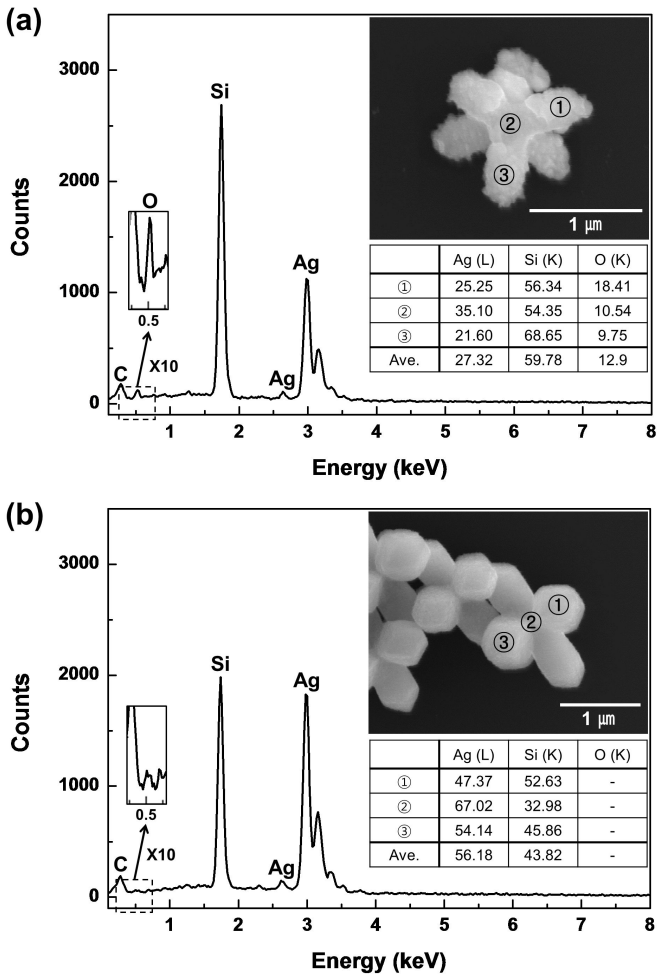

Figure 2. Energy dispersive spectrum of a Ag_2O quasi-hexapod (a) or Ag hexapod (b) obtained from the area designated as "①" in each particle. The oxygen peak is clearly shown in the magnified (´10) spectrum of (a), while it is not observed in (b). The atomic % ratio of Ag, O, and Si is obtained at three different areas designated as "①", "②", and "③" in the inset of (a) or (b). The averaged atomic % ratio of Ag, O, and Si for each particle is 27.3%, 12.9%, and 59.78% for the Ag_2O quasi-hexapod or 56.18%, 0%, and 43.82% for the Ag hexapod, respectively.

SEM images whether the finally obtained hexapods (Fig. 1b) are composed of Ag, resulting from the reduction of Ag_2O hexapods. To verify the reduction,

compositional analysis was carried out on both hexapods (Ag_2O and Ag) using energy dispersive spectroscopy (EDS) equipped with SEM. Both EDS spectra obtained at site ① of the Ag_2O (inset of Fig. 2a) and Ag (inset of Fig. 2b) hexapod showed characteristic X-ray peaks of Ag, Si, and C. On the other hand, the O peak is shown only in Fig. 2a and not in Fig. 2b, meaning that the Ag_2O hexapod is successfully reduced into the Ag hexapod. Two EDS spectra of both hexapods were additionally taken at different sites, designated as ② and ③, to investigate the site-dependence of the EDS spectra. All three spectra obtained at the three different sites of each Ag_2O and Ag hexapods represent the same aspect. The O peak appears only in the EDS spectra of the Ag_2O hexapod.

The efficiency of the X-ray detector in the EDS system is significantly decreased in the low energy region, because low energy X-rays below ~0.7 eV (K_α lines emitting from light elements) are efficiently absorbed by the beryllium window in front of the detector. Because of this large absorption of low energy X-rays, it is difficult to find the exact correction models for light elements. This disadvantage of EDS raises some concerns about the accuracy of the quantitative analysis of the EDS data. Thus, for further confirmation, the X-ray diffraction (XRD) pattern for the Ag hexapods was obtained (Fig. 3a) and compared with the standard characteristic peaks of Ag (Fig. 3b). The typical XRD pattern for the Ag hexapods shows four characteristic peaks at 38°, 44°, 64.6°, and 77.5° that correspond to those of standard Ag (JCPDS 04-0783) and can be assigned to reflections from the (111), (200), (220), and (311) planes, respectively. The XRD pattern of the Ag_2O hexapods is also presented in Fig 3c. Three peaks were observed at 33°, 38°, and 55°, representing the (111), (200), and (220) planes of traditional Ag_2O, respectively (Fig. 3d, JCPDS 12-0793). Comparing the XRD patterns for the Ag and Ag_2O hexapods clearly

reveals that the contents of the hexapods particles shown in Fig. 1a and b are Ag_2O and Ag, respectively. This result also shows that Ag_2O was successfully reduced to Ag by $NaBH_4$ while preserving the morphology.

X-ray photoelectron spectroscopy (XPS) is another powerful technique that can be used to identify Ag hexapods. The XPS spectrum obtained from the Ag

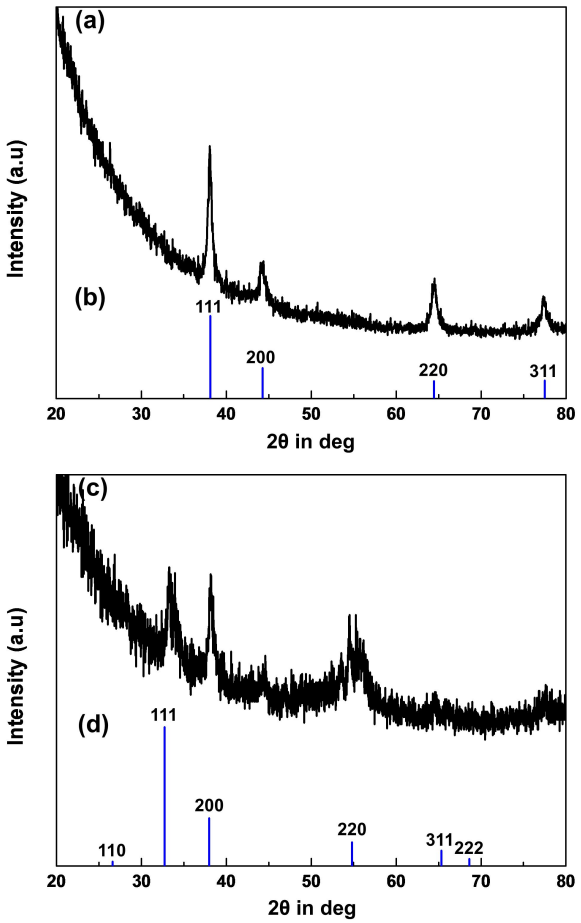

Figure 3. X-ray diffraction pattern for Ag hexapod (a), or Ag_2O quasi-hexapod (c). Four characteristic peaks at 38 , 44 , 64.6 , and 77.5 in (a) correspond to the typical XRD pattern of standard Ag (JCPDS 04-0783) (b), and each peak represents (111), (200), (220), and (311) plane, respectively. The Ag_2O quasi-hexapods show three peaks at different angles, 33 , 38 , and 55 , that can be assigned into (111), (200), and (220), according to those of Ag_2O (JCPDS 12-0793).

hexapods (Fig. S3a) shows two peaks, at 367.6 and 373.5 eV, that correspond to the binding energies (BEs) of Ag $3d_{5/2}$ and $Ag3d_{3/2}$, respectively. These two values are much lower than the BEs of pure Ag^0 (368.3 and 374.3 eV) reported previously[31]. Contrary to the BE of Ag 3d, the O 1s peak originating from the oxygen of TSC appears at 532.1 eV (Fig. S3b) and is much larger than the literature value (530.3 eV)[32]. The red shift of Ag 3d and the blue shift of O 1s indicate that the Ag atoms on the surface of the Ag hexapods strongly coordinate with the O atoms of TSC. According to previous literature, the reported BE of Ag $3d_{5/2}$ in Ag_2O wires is 367.9 eV[33]. Because this value is very close to 367.6 eV, which is our measured BE of Ag $3d_{5/2}$ for the Ag hexapods, XPS contributes little to the characterization.

The optical properties of the Ag_2O and Ag hexapods should be different, because Ag_2O is a semiconductor with a band gap, and its electronic band structure is completely different from metallic Ag. Because the reported band

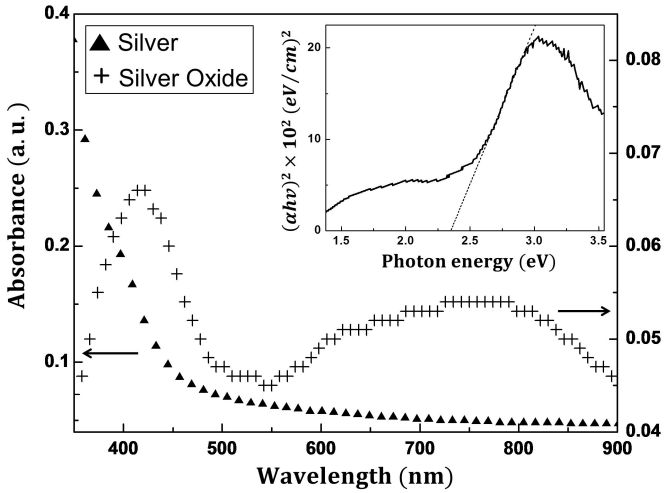

Figure 4. UV-Vis absorption spectrum of Ag hexapods (filled triangle dots) is completely different from that of Ag_2O quasi-hexapods (cross dots). The band gap of Ag_2O quasi-hexapods can be estimated from the Tauc plot (the inset) by extrapolating the linear portion of the curve (dotted line in the inset) to the X-axis. The band gap is given as the value of the X-intercept (2.35 eV).

gap of Ag_2O ranges from 1.3 to 2.27 eV, which corresponds to the energy of visible light, the Ag_2O hexapods will show an apparent band to band transition (from valence to conduction band) in the range of visible light[34-37]. Fig. 4 shows the UV-Vis absorption spectra for the Ag_2O (cross dots) and Ag hexapods (filled triangles). The Ag_2O hexapods show two strong absorption bands in around 430 and 750 nm, whereas no distinctive absorption band appears in long-wavelength-range of the spectrum for the Ag hexapods. Although no band to band transition occurs in metallic Ag hexapods, the surface plasmons (SPs) of Ag hexapods can be excited by light irradiation. The resonance wavelength of SPs for nanoparticles is strongly dependent on their size. As the size of the nanoparticle increases, the resonance energy of SPs generally moves to longer wavelengths. Because the average size of the Ag hexapods is 300-1000 nm, low frequency SPs are far from the visible light region, and only multipoles of SPs are observed in the visible range (~400 nm) of the spectrum for the metallic Ag hexapods. The band gap of the Ag_2O hexapods can be estimated using a Tauc plot (inset of Fig. 4), which is obtained from the UV-Vis absorption spectrum of the Ag_2O hexapods. Assuming that the Ag_2O hexapods are direct transition-type semiconductors[34-37], we can replace the unit of the Y-axis with "$(\alpha h\nu)^2$", where "$h\nu$" is the incident photon energy, and "α" is the absorption coefficient calculated from absorbance (A) and the optical path length (l) using equation (1). The linear portion of the curve in the inset of Fig. 4 is fitted using Tauc equation (2) (dotted line in the inset of Fig. 4). When $(\alpha h\nu)^2 = 0$, the band gap (E_g) is 2.35 eV, which is intercept of the X-axis, as shown in the inset of Fig. 4.

$$\alpha = \frac{2.303 \cdot A}{\ell} \quad (1)$$

$$(\alpha h\nu)^2 \propto (h\nu - E_g) \quad (2)$$

The reported band gap energy of Ag_2O is diverse, ranging from 1.3 to 2.27 eV, according to its method of preparation. For example, the band gap energy of Ag_2O films prepared by electrodeposition is 1.46 eV[35], while Ag_2O films deposited through reactive magnetron sputtering show a higher band gap energy[37], 2.27 eV, which is similar to the value of 2.35 eV measured in our experiment. Because the different stoichiometries between Ag and O can partially cause an increase in the band gap energy, one might suspect the existence of different forms of silver oxide such as AgO, Ag_3O_4, Ag_4O_3, and Ag_2O_3; however, the major chemical form in Fig. 1a is Ag_2O, because Ag_2O is the most thermodynamically stable[38].

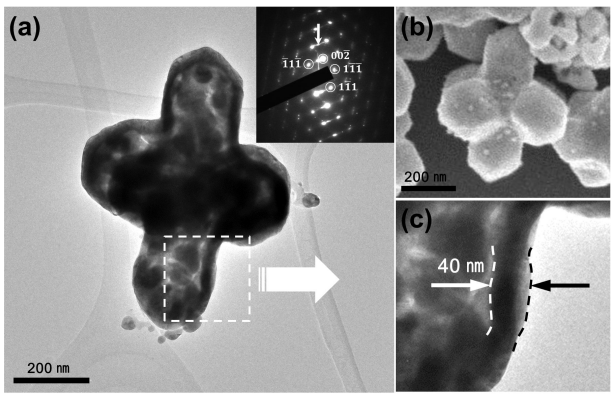

Figure 5. The contrast of the transmission electron micrograph (a) is not uniform, even though the outer surface is smooth, as shown in the scanning electron micrograph (b). This means that the Ag hexapod has a partially hollow inner structure. The selective area diffraction (SAED) pattern (the inset of (a)) was obtained for the entire area of the Ag hexapod shown in (a). Several dots with streaking lines in the SAED pattern represent a single crystalline phase with a planar defect. On closer inspection, the Ag hexapod is covered with a shell-like structure. This shell-like structure is clearly seen in (c), which is the magnified image of the dashed box in panel (a). The thickness of the shell-like structure is measured to be ~ 40 nm.

According to the mechanism suggested by Huang et al.[25], quasi-spherical Ag_2O particles are reduced and transformed into hollow Ag spheres using a reducing agent, $NaBH_4$. They explained that Ag atoms or clusters reduced from

Ag_2O emigrate to the outer surfaces through channels created by hydrogen gas to form shell-like structures on the surface of the Ag_2O quasi-spheres. We hypothesize that the same mechanism is applicable to our system (Ag hexapods), so we expect the Ag hexapods to also have hollow structures. To investigate the inner structures of the Ag hexapods, we employed transmission electron microscopy (TEM). A typical TEM image of a Ag hexapod is shown in Fig. 5a. The contrast in overall structure is not uniform, which means that the thickness is different along the Ag hexapod. Because the outward surface of the Ag hexapod is smooth (Fig. 5b), the difference in contrast results from the partially hollow inner structure of the Ag hexapod. In addition, this shell-like structure is also observed in the outermost region of the hexapod. A close-up of the boxed region distinctly shows that a shell ~40 nm thick (Fig. 5c) was formed on the outside of the Ag hexapod. The selective area electron diffraction (SAED) pattern for the whole structure of the Ag hexapod was obtained (inset of Fig. 5a) and compared with four different SAED patterns obtained for each branch (Fig. S4). In all the SAED patterns, a set of diffraction spots are observed with characteristic streaking (white arrow in the inset of Fig. 5a), which means that the Ag hexapod has a single crystalline phase with {111} planar defects. Several Ag hexapods were selected, and they showed the same result. Fig. S5a shows another representative TEM image and its SAED pattern (the inset). It shows that the Ag hexapod is a single crystal with a partially hollow inner structure and a shell-like structure in the outer portion of the hexapod (Fig S5c). The zone axis of Fig 5a is [110], which is calculated from the SAED pattern in the inset of Fig. 5a. The zone axis, [110], and the square cross-sectional shape of each branch (Fig S5b) reveal that the side faces of each branch are bounded by the {110} faces, and the sharp-faced tip is bounded by the {111} tip faces[27].

5. Conclusion

In this paper, we introduced a novel scheme to synthesize Ag hexapods from Ag_2O quasi-hexapods. In this scheme, Ag_2O quasi-hexapods are initially prepared by decreasing the reaction rate using BSPP as a ligand, and the as-prepared Ag_2O quasi-hexapods are reduced to Ag hexapods using $NaBH_4$. The shape of the Ag_2O (quasi-hexapods) is not changed during the reduction, resulting in well-defined Ag hexapods. The reduced Ag atoms or clusters produced inside the Ag_2O hexapods migrates from the inside to the outside to form a shell on the surface of the Ag_2O hexapods, resulting in partially hollow Ag hexapods. This proves that Ag_2O can act as a template for the synthesis of partially hollow Ag nanoparticles, and the general application of this method will be used to synthesize a wider variety of Ag nanoparticles that cannot be prepared using conventional methods such as the galvanic replacement reaction method.

6. References

[1] Rosi, N.L.; Mirkin, C.A. *Chem. Rev.* **2005**, *105*, 1547-1562.

[2] Anker, J.N.; Hall, W.P.; Lyandres, O.; Shah, N.C.; Zhao, J.; Duyne, R.P.V. *Nat. Mater.* **2008**, *7*, 442-453.

[3] Lal, S.; Link, S.; Halas, N.J. *Nature Photon.* **2007**, *1*, 641-648.

[4] Leenen, M.A.M.; Arning, V.; Thiem, H.; Steiger, J.; Anselmann, R. *Phys. Status Solidi A.* **2009**, *206*, 588-597.

[5] Xie, J.; Lee, J.; Chen, X. *Adv. Drug Deliv. Rev.* **2010**, *62*, 1064-1079.

[6] Rosi, N.L.; Giljohann, D.A.; Thaxton, C.S.; Lytton-Jean, A.K.R.; Han, M.S.; Mirkin, C.A. *Science.* **2006**, *312*, 1027-1030.

[7] Daniel, M.-C.; Astruc, D. *Chem. Rev.* **2004**, *104*, 293-346.

[8] Burda, C.; Chen, X.; Narayanan, R.; El-Sayed, M.A. *Chem. Rev.* **2005**, *105*, 1025-1102.

[9] Turkevich, J.; Stevenson, P.C.; Hillier, J. *Faraday Soc.* **1951**, *51*, 55-75.

[10] Sun, Y.; Gates, B.; Mayers, B.; Xia, Y. *Nano Lett.* **2002**, *2*, 165-168.

[11] Martin, C.R. *Science.* **1994**, *266*, 1961-1966.

[12] Jin, R.; Cao, Y.; Mirkin, C.A.; Kelly, K.L.; Schatz, G.C.; Zheng, J.G. *Science.* **2001**, *294*, 1901-1903.

[13] Sun, Y.; Xia, Y. *Science.* **2002**, *298*, 2176-2179.

[14] Zhang, J.; Li, S.; Wu, J.; Schatz, G.C.; Mirkin, C.A. *Angew. Chem. Int. Ed.* **2009**, *121*, 7927-7931.

[15] Zhou, J.; An, J.; Tang, B.; Xu, S.; Cao, Y.; Zhao, B.; Xu, W.; Chang, J.; Lombardi, J.R. *Langmuir.* **2008**, *24*, 10407-10413.

[16] Seo, D.; Park, J.C.; Song, H. *J. Am. Chem. Soc.* **2006**, *128*, 14863-14870.

[17] Pietrobon, B.; Kitaev, V. *Chem. Mater.* **2008**, *20*, 5186-5190.

[18] Chen, S.; Fan, Z.; Carroll, D.L. *J. Phys. Chem. B.* **2002**, *106*, 10777-10781.

[19] Hao, E.; Kelly, K.L.; Hupp, J.T.; Schatz, G.C. *J. Am. Chem. Soc.* **2002**, *124*, 15182-15183.

[20] Jana, N.R.; Gearheart, L.; Murphy, C.J. *Chem. Commun.* **2001**, *7*, 617-618.

[21] Zhang, D.; Qi, L.; Ma, J.; Cheng, H. *Chem. Mater.* **2001**, *13*, 2753-2755.

[22] Sun, Y.; Mayers, B.; Xia, Y. *Adv. Mater.* **2003**, *15*, 641-646.

[23] Lim, J.K.; Ciszek, J.W.; Huo, F.; Jang, J.-W.; Hwang, S.; Mirkin, C.A. *Nano Lett.* **2008**, *8*, 4441-4445.

[24] Sun, Y.; Liu, Y.; Zhao, G.; Zhang, Q. *Nanoscale Res. Lett.* **2008**, *3*, 82-86.

[25] Yang, P.; Zhang, Y.; Huang, B. *Mater. Res. Bull.* **2013**, *48*, 3756-3760.

[26] Jelić, D.; Penavin-Škundrić, J.; Majstorović, D.; Mentus, S. *Thermochim. Acta* **2011**, *526*, 252-256.

[27] Lyu, L.-M.; Wang, W.-C.; Huang, M.H. *Chem. Eur. J.* **2010**, *16*, 14167-14174.

[28] Kim, M.-J.; Cho, Y.-S.; Park, S.-H.; Huh, Y.-D. *Cryst. Growth Des.* **2012**, *12*, 4180-4185.

[29] Wang, X.; Wu, H.-F.; Kuang, Q.; Huang, R.-B.; Xie, Z.-X.; Zheng, L.-S. *Langmuir.* **2010**, *26*, 2774-2778.

[30] Xue, C.; Métraux, G.S.; Millstone, J.E.; Mirkin, C.A. *J. Am. Chem. Soc.* **2008**, *130*, 8337-8344.

[31] Gao, Y.; Jiang, P.; Liu, D.F.; Yuan, H.J.; Yan, W.Q.; Zhou, Z.P.; Wang, J.X.; Song, L.; Liu, L.F.; Zhou, W.Y.; Wang, G.; Wang, C.Y.; Xie, S.S.; Zhang, J.M.; Shen, D.Y. *J. Phys. Chem. B.* **2004**, *108*, 12877-12881.

[32] Liu, X.; Zhang, F.; Huang, R.; Pan, C.; Zhu, J. *Cryst. Growth Des.* **2008**, *8*, 1916-1923.

[33] Murray, B.J.; Newberg, J.T.; Walter, E.C.; Li, Q.; Hemminger, J.C.; Penner, R.M. *Anal. Chem.* **2005**, *77*, 5205-5214.

[34] Tjeng, L.H.; Meinders, M.B.; van Elp, J.; Ghijsen, J.; Sawatzky, G.A. *Phys. Rev. B.* **1990**, *41*, 3190-3199.

[35] Ida, Y.; Watase, S.; Shinagawa, T.; Watanabe, M.; Chigane, M.; Inaba, M.; Tasaka, A.; Izaki, M. *Chem. Mater.* **2008**, *20*, 1254-1256.

[36] Saroja, G.; Vasu, V.; Nagarani, N. *Open Journal of Metal.* **2013**, *3*, 57-63.

[37] Pierson, J.F.; Wiederkehr, D.; Billard, A. *Thin Solid Films.* **2005**, *478*, 196-205.

[38] Feng, H.-L.; Gao, X.-Y.; Zhang, Z.-Y.; Ma, J.-M. *J. Korean Phys. Soc.* **2010**, *56*, 1176-1179.

Chapter Two.

A New Approach to Obtain Correct and Simplified Equation Applied to Inner Space Assessment for Capsule-like Superstructures

1. Abstract

Polypyrrole-Gold (PPy/Au) segment nanowires are prepared using anodized aluminum oxide (AAO) templates and assembled into a curved superstructure. Since the shape of the obtained superstructures can be designed to be capsule-like with inner space for containing materials, and their openings and closures can be controlled with external stimuli, these structures can be useful for a large variety of applications. Inner space of capsule-like superstructures is an important factor for their applications, and the volume of the inner space can be assessed using the generalized equation suggested by J. K. Lim (Bull. Korean Chem. Soc. 33, 2699 (2012)). In this paper, we introduce a new approach to obtain correct and simplified equation without redundant assumption which was used to induce the previous equations, and recalculate the volume of the inner space in the capsule-like superstructure using a new equation.

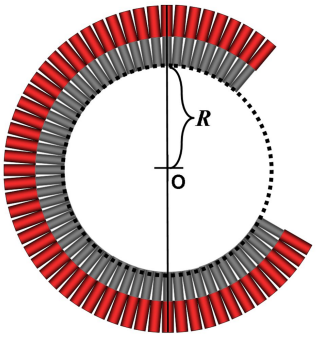

with assumption

$$R = \frac{d_{Au}}{\alpha} - l_{PPy}, \quad \alpha = 2\tan^{-1}\left(\Delta d / 2l_{PPy}\right)$$

$$R = \frac{d_{PPy} + \Delta d\cos(\alpha/2)}{\alpha} - l_{PPy}, \ \alpha = 2\tan^{-1}\left(\Delta d / 2l_{PPy}\right)$$

without assumption

$$R = \frac{d_{PPy} \cdot l_{PPy}}{\Delta d}$$

2. Introduction

Polypyrrole-Gold (PPy/Au) segment nanowires are prepared within the pores of anodized aluminum oxide (AAO) templates and assembled owing to capillary and van der Waals forces following which AAO templates are placed in aqueous sodium hydroxide solution and the water is evaporated (Scheme 1(a), 1(b), 1(c)). The obtained superstructures are rolled up to form a curved superstructure with further evaporation of the water from the matrix of PPy segment that makes the diameter of the PPy segment smaller than that of the Au segment (Scheme 1d).[1,2] Traditional photolithographic technique allows curved superstructures to be complete capsule-like superstructures with inner space available for containing materials.[2,3] Recently, it has been reported that opening and closure of curved superstructure can be controlled by external stimuli, such as humidity, temperature, and light.[4] This actuation can be explained by the change of PPy segment volume, which is increased (or decreased) by absorbing (or desorbing) the water vapor that makes the curved superstructure expand (or shrink), accordingly (Scheme 1(d), 1(e)). Remotely-controlled capsule-like superstructures can be used for a large variety of applications (e.g. microcapsules, microreactors, and delivery systems).

The radius of the inner space in the capsule-like superstructure can be assessed using simple equation suggested in the previous paper (Eq. 1).[4]

$$R = \frac{d_{Au}}{\alpha} - l_{PPy},\ \alpha = 2\tan^{-1}(\triangle d / 2l_{PPy}) \qquad (1)$$

According to the equation, the radius of the inner space (R) is determined by the length of PPy (l_{PPy}), the diameter of Au (d_{Au}), the diameter of PPy (d_{PPy}), and the diameter difference between Au and PPy segments ($\Delta d = d_{Au} - d_{PPy}$). This equation yields good results under assumption that the length of the PPy segment is comparable or much longer than that of the Au segment. In recent

paper, the equation was modified, and generalized for all lengths of the PPy segment (Eq. 2).[5]

$$R = \frac{d_{PPy} + \Delta d \cos(\alpha/2)}{\alpha} - l_{PPy},\ \alpha = 2\tan^{-1}(\Delta d / 2l_{PPy}) \qquad (2)$$

In both equations (1 and 2), however, the radius of the inner space is induced from the circumference of hypothetical circle (dotted circle in Fig. 1(a)). In this paper, we discard this redundant assumption, and introduce a new equation for better assessing the volume of the inner space.

3. Derivation of New Equation

Let the radius of the inner space in the capsule-like superstructure as R (Fig. 1(a)). Angle α (∠AOC Fig. 1(b)) is the included angle between the two adjacent wires. AC (Fig. 1(b), (c)) is the segment connecting the centers of the ends of the two adjacent PPy (Fig. 1(c)). The angle ∠AOD is the same as ∠BAD (Fig. 1(c)) and amounts to α/2, because ΔOAB equals to ΔABD. The length of AD, defined as y, is calculated either from ΔOAD or from ΔABD (Eq. 3).

$$y = R \cdot \sin(\frac{\alpha}{2}) = \frac{d_{PPy}}{2} \cdot \cos(\frac{\alpha}{2}) \qquad (3)$$

Eq. (3) can be converted using a tangent function, and tan(α/2) can be replaced with Δd, the difference of diameters between the PPy and the Au segment and l_{PPy} (Eq. 4).[4]

$$\tan(\frac{\alpha}{2}) = \frac{\Delta d}{2l_{PPy}} \qquad (4)$$

Finally, the radius of the inner space, R is represented with only variables, d_{PPy}, l_{PPy} and Δd (Eq. 5).

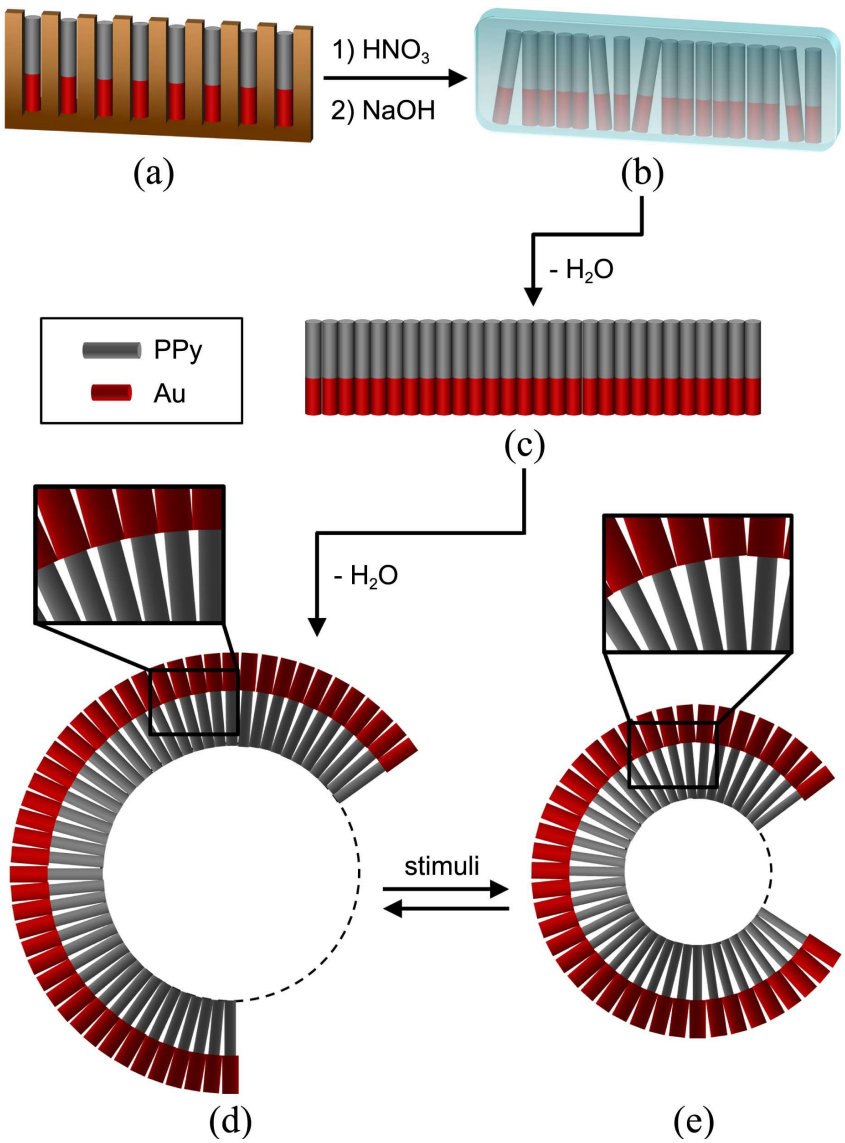

Scheme 1. Schematic picture representing the procedure for forming the curved superstructures through the guidance of anodized aluminum oxide templates, (a, b, c, and d), and their opening and closure by external stimuli (d and e).

$$R = \frac{d_{PPy} \cdot l_{PPy}}{\Delta d} \quad (5)$$

4. Results and Discussion

The radius of the inner space in capsule-like superstructure R is a function of Δd which is variable value from 20 to 60 nm.[1-4] This range depends on environmental conditions, such as temperature, humidity, and light intensity. R is calculated at different length of the PPy segment (l_{PPy}) using Eqs. (1), (2), or (5), under the assumption that Δd falls in the above range, and then plotted against to l_{PPy} (Fig. 2(a), 2(b)). When Δd equals 20 nm, R calculated with Eq. (2) (dotted line in Fig. 2(a)) is almost the same as calculated with Eq. (1) (dashed line in Fig. 2(a)) At all length of the PPy segment, however, Eq. (5) shows better results (solid line in Fig. 2(a)) which is slightly less than that calculated from Eq. (1) and (2). On the other hand, when Δd becomes 60 nm, R calculated with Eq. (2) (dotted line in Fig. 2(b)) is slightly different, while R calculated with Eq. (5) (solid line in Fig. 2(b)) is significantly different from that calculated with Eq. (1) (dashed line in Fig. 2(b)), as the length of PPy segment decreases.

This difference can be clearly seen in Figure 2(c) where the difference of radii from different equations is plotted against l_{PPy}. In Figure 2(c), filled and blank marks show the difference of radii when Δd equals 20 or 60 nm, respectively. In the case of small Δd (Δd = 20 nm), the difference of radii (filled diamonds, or squares in Fig. 2(c)) gradually increases. On the other hand, when Δd is 60 nm, difference of radii calculated with Eqs. (1), (2), and (5) shows distinctly increased behavior, as l_{PPy} becomes below 1000 nm (empty diamonds, or squares in Fig. 2(c)).

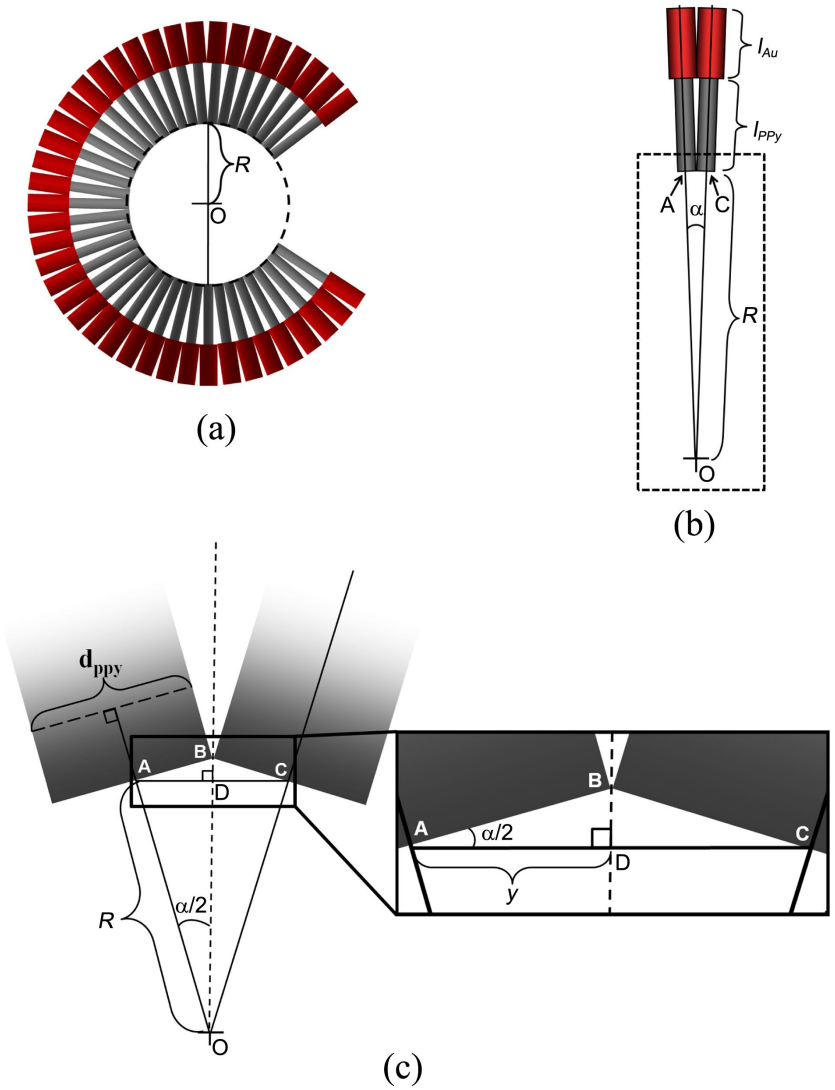

Figure 1. Schematic picture of the curved superstructure, (a), and its magnified image, (b). Dashed area of (b) is highlighted in (c).

Since capsule-like superstructures have inner space where materials can be contained and released outside in a controllable manner, capsule-like superstructures examined in this report can be used in a number of novel

microencapsulation applications. The important requirement to this end is the available volume of the inner space. The available volume can be calculated from the radius of the inner space using Eqs. (1), (2) or (5) when Δd is 20 or 60 nm (Fig. 3 or 4). Since the radius of inner space is increased with l_{PPy} as shown in Figure 2(a), (b), the volume of inner space is also increased with l_{PPy} (Fig. 3(a), and 4(a)). In Figure 2(a), (b), the rate of change for radius is nearly independent on l_{PPy}, but the rate of change for volume is completely depending on l_{PPy} in Figure 3(a), and 4(a). In addition, the rate of change for volume varies with the used equations (Fig. 3(b), (c), and 4(b), (c)). As the length of PPy is increased, the difference of volume is also increased. The difference of volume (the distances between lines in Fig. 3(b) and 4(b)) in the middle length of PPy is smaller than that in long PPy (the distances between lines in Fig. 3(c) and 4(c)). This trend means that the rate of change for the volume is dependent on not only the length of PPy but also used equations.

There are big differences between radius and volume. In Figure 2(c), the difference of radius calculated using three equations is increased as the length of PPy segment is decreased, however, the volume of the inner space show completely different results in Figure 5, where the difference of volume increases with l_{PPy}. This trend is shown not only at small Δd (filled marks) but also at large Δd (blank marks) in Figure 5. In addition, while the difference of volume is rapidly increased at small Δd more than that at large Δd in Figure 5, the difference of radius is rapidly changed at large Δd more than that at small Δd in Figure 2(c). This discrepancy between radius and volume apparently seems to be opposite, but we should consider that the volume is proportional to the the 3^{rd} power of the radius ($V \propto r^3$). In addition, we plotted not the radius (r) or volume (V) itself but the difference of radius (Δr) or volume (ΔV) in Figure 2 or 5, respectively. Although the difference of radius is decreased as the length of PPy is increased as shown in Figure 2(c), the difference of

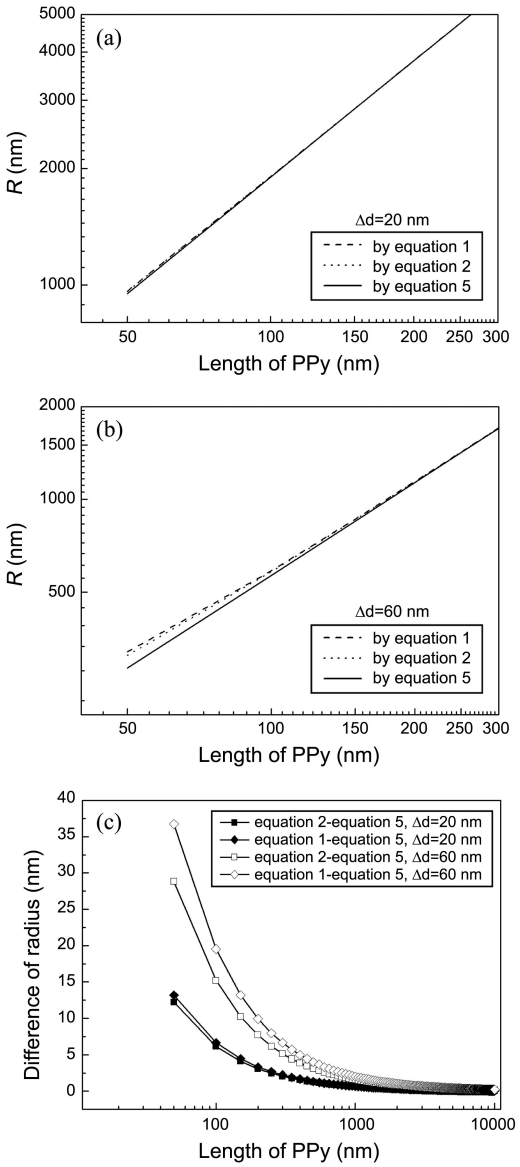

Figure 2. The radius of inner space, R was calculated using Eqs. (1), (2), or (5), and plotted against to the length of polypyrrole segment, l_{PPy}, when the difference of diameter between gold and polypyrrole segment, Δd is 20 nm, (a), and 60 nm, (b). As l_{PPy} is decreased, R is also decreased in both (a) and (b), but the difference of radius (R from Eq. (1) - R from equation 2 or 5) in (b) is larger than that in (a), and which is clearly seen in (c). As increasing of l_{PPy}, the difference of radius of inner space is increased.

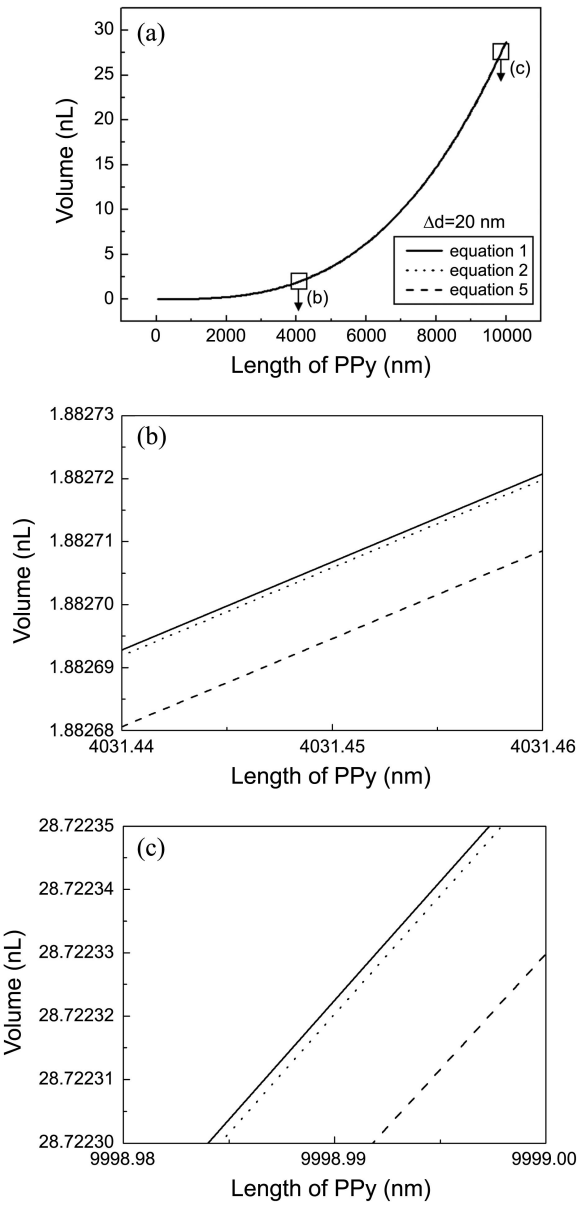

Figure 3. The volume of inner space calculated using Eqs. (1), (2), or (5) in small Δd (Δd = 20 nm) is increased, as the length of PPy is increased, (a). The difference of volume is also increased with increasing of the length of PPy, which is clearly seen in (b), and (c). The difference of volume at long PPy (distance between lines in (c)) is larger than that at short PPy (distance between lines in (b)).

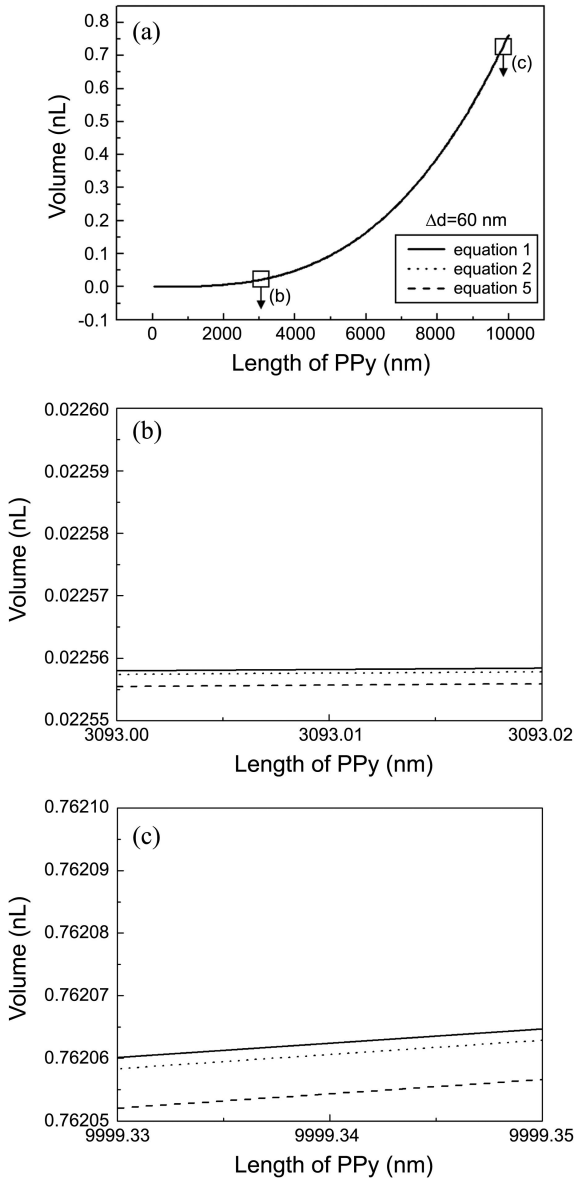

Figure 4. The volume of inner space calculated using equation 1, 2, or 5 in large Δd (Δd = 60 nm) is increased, as the length of PPy is increased, (a). The difference of volume is also increased with increasing of the length of PPy, which is clearly seen in (b), and (c). The difference of volume at long PPy (distance between lines in (c)) is larger than that at short PPy (distance between lines in (b)).

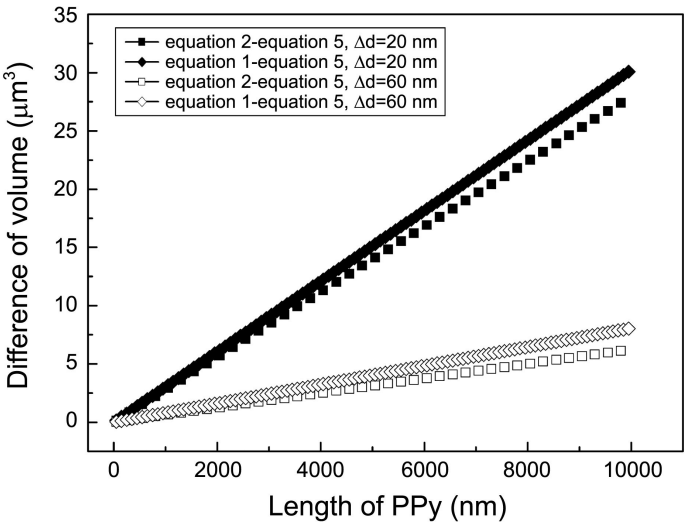

Figure 5. The difference of volume calculated equation 1, 2, or 5 is plotted against to the length of PPy. The difference of volume in small Δd (filled squares or diamonds) is rapidly increased more than the difference of volume in large Δd (empty squares or diamonds), with increasing of the length of PPy.

volume can be increased with increasing of the length of PPy (Figure 5). This apparently opposite trend is mathematically natural result, but shows that small difference of radius can make large volume difference. Eq. (5) newly suggested in this manuscript is much simpler than the previously suggested equations (Eqs. (1) and (2)), and mathematically complete equation, because redundant assumption is excluded.

5. Conclusion

In this paper, we adopted a new approach to obtain new equation which is much simpler than the previous equations. In addition, since this new equation was derived without redundant assumption, the new equation is accurate more than the two previous equations, and acceptable at all lengths of l_{PPy}. The volume and radius of the inner space of the capsule-like superstructure were calculated using three equations and compared with each other. The radii of inner space show small deviation from each to each, however, the volumes of the inner space show large difference as l_{PPy} increases. The assessment of the available volume is very important for practical applications of capsule-like assembled superstructures, such as microencapsulation.

6. References

[1] Park, S.; Lim, J.-H.; Chung, S.-W.; Mirkin, C. A. Science 2004, 303, 348.

[2] Ciszek, J. W.; Huang, L.; Wang, Y.; Mirkin, C. A. Small 2008, 4, 206.

[3] Ciszek, J. W.; Huang, L.; Tsonchev, S.; Wang, Y.; Shull, K. R.; Ratner, M. A.; Schatz, G. C.; Mirkin, C. A. ACS Nano 2010, 4, 259.

[4] Lim, J. K.; Ciszek, J. W.; Huo, F.; Jang, J.-W.; Hwang, S.; Mirkin, C. A. Nano Lett. 2008, 8, 4441.

[5] Lim, J. K. Bull. Korean Chem. Soc. 2012, 33, 2699.

감사의글

학부생 3학년 때부터 지금까지, 랩 생활을 시작한지가 엊그제 같은데 벌써 4년이라는 시간이 흘렀습니다. 제게 4년이라는 시간은 정말 감사함으로 가득한 시간이었습니다.

먼저 아무것도 모르는 저를 열정과 애정으로 지도하여 이만큼 성장시켜주신 저의 지도교수님이신 임종국 교수님께 감사인사를 드립니다. 짧지 않은 시간동안 교내에서, 또 일본의 IMS에서 많은 기회와 가르침을 주심에 깊은 감사를 드리며 학교를 떠나서도 교수님의 가르침대로 성실하게 끊임없이 연구하는 연구원이 되겠습니다.

그리고 바쁘신 가운데에도 제 학위논문 심사를 맡아주시고 좋은 조언해주신 손홍래 교수님과 김호중 교수님께도 감사의 말씀 드립니다. 또한 다방면으로 지도 편달 해주신 화학과 모든 교수님들께도 감사드립니다.

랩 생활을 하며 희노애락을 함께 한 NSL식구들, 형주오빠, 다솔이, 윤정이에게도 고맙다는 인사를 하고 싶습니다. 그리고 심적으로 많은 의지가 되었던 MOC 선배들과 동기인 유진이언니와 혜선이에게 감사를 전하며, 앞으로도 좋은 우정을 이어나가고 싶습니다.

마지막으로, 항상 저를 믿어주시고 응원해주시는 정신적 지주인 사랑하는 제 가족에게 큰 감사인사를 올립니다. 은혜에 보답할 수 있는 자랑스러운 딸이 되도록 노력하겠습니다.